

High-fidelity robust qubit control by phase-modulated pulses

Marko Kuzmanović , Isak Björkman , John J. McCord , Shruti Dogra , and Gheorghe Sorin Paraoanu ^{*}

InstituteQ and QTF Centre of Excellence, Department of Applied Physics, School of Science, Aalto University, FI-00076 Aalto, Finland



(Received 15 September 2023; accepted 23 January 2024; published 21 February 2024)

We present a set of *robust* and *high-fidelity* pulses that realize paradigmatic operations such as the transfer of the ground state population into the excited state and arbitrary X/Y rotations on the Bloch sphere. These pulses are based on the phase modulation of the control field. We provide an experimental proof-of-concept of these operations by using a transmon qubit, demonstrating resilience against deviations in the drive amplitude of more than $\approx 20\%$, and/or detuning from the qubit transition frequency in the order of 10 MHz. This modulation scheme is straightforward to implement in practice and can be deployed to any other qubit-based experimental platform.

DOI: [10.1103/PhysRevResearch.6.013188](https://doi.org/10.1103/PhysRevResearch.6.013188)

I. INTRODUCTION

Quantum control—a toolbox of techniques enabling high-fidelity dynamical operations—is an essential tool in modern quantum technologies. Perhaps the first example of quantum control is the 1932 Rosen-Zener sech-function design of the shape of the rate of rotation of the magnetic field in a double Stern-Gerlach experiment [1]. In contrast to designing the shape of the pulse envelope, changing its phase or frequency is a less explored avenue. While simple forms of modulation (linear, sinusoidal, square) have been studied experimentally [2], this has confined the use of this concept to repetitive passages, which have the benefit that interference effects can be observed in a straightforward way. However, recent advances in modern electronics have enabled the precise manipulation of the pulse phases in the time domain. This allows the formulation of quantum control schemes where the phase is an externally controlled parameter.

An outstanding problem that can be addressed by these methods is the realization of high-fidelity gates and other operations in superconducting qubits, one of the most promising platforms for quantum computing and simulation. Compared to other well-established experimental platforms, superconducting qubits present an additional specific set of challenges. Since these are artificial atoms comprising several materials and complex geometries, it is in general not possible to provide a sufficiently accurate and complete mathematical model describing the system. Losses and unaccounted-for interactions inevitably lead to errors when using simplified models. To combat this several concepts have been proposed and applied recently: for example, error mitigation

(extrapolation to zero-noise limit or probabilistic error cancellation) [3–5], Pauli and Clifford twirling [6,7], derivative removal by adiabatic gate [8–10], dynamical decoupling [11–13], counterdiabatic methods [14–18], composite pulses [19–22], and more recently reinforcement learning [23–31]. There is however no universal solution, as each of these methods comes with its own disadvantages. For example, machine-learning techniques typically require discretized forms of multiple control parameters, which complicates their synthesis by standard control systems. While this problem may be alleviated in the future by the use of cryogenic control systems, for example Josephson arbitrary wave-form synthesizers [32], such pulses may still have a power spectrum leading to spurious excitations in a larger, frequency-crowded device. Composite pulses can, in general, be effective for mitigating errors in the Rabi frequency and even protect against frequency shifts [33] but the concatenated series of pulses may take a long time, allowing decoherence to take its toll.

Also, techniques that require a very precise shape optimization of pulses may not be so effective, since microwave pulses will be inevitably distorted when transmitted to the qubit, and finding the exact transfer function requires further extensive calibrations [34–36]. Another solution could be to use a closed-loop approach based on randomized benchmarking of a subset of gates [37], a method that can be extended to include leakage control with tens of parameters to optimize [38]. However, as the shape of the pulse becomes more complex, a large number of parameters are needed, and the optimization time may increase significantly [38]. An alternative solution is to use geometrical optimization concepts, which can result in rather low pulse areas and slow modulations of parameters [39–41], at the expense of a more complicated implementation.

Here we show that by chirping the frequency of the pulses according to relatively simple and smooth functions, we can achieve gates that are robust against both amplitude and frequency errors. We restrict the power of the microwave pulse in order to avoid exciting other modes due to frequency crowding, also to limit the effect of nonlinearities in microwave

^{*}sorin.paraoanu@aalto.fi

components (especially mixers at room temperature) and in the on-chip circuit elements (other nearby qubits, modes, etc.) that may lead to frequency shifts that are not accounted for in calibration. Combined with the requirement of minimizing the time of the operation, this inevitably leads to pulses that are close to rectangular.

We demonstrate this by implementing two paradigmatic operations: transfer of population from one level to another and arbitrary rotations on the Bloch sphere. In both cases, the experimental data are supported by simple theoretical models and by numerical simulations that include only parameters extracted from independent characterization measurements.

These control techniques are validated in a setup comprising a transmon qubit, although the methods developed here are, in principle, hardware-agnostic. Besides robustness and high-fidelity, which will be substantiated further, a great advantage of our scheme is simplicity: we work with a small number of optimization parameters: the rate of the frequency variation for the first task and a few Fourier coefficients for the second one, which makes the optimization very efficient numerically.

Our results on population transfer and rotation gates have immediate applications in a wide array of quantum-information tasks realized with superconducting circuits or on other quantum platforms.

First, population transfer is an important operation in quantum information processing, as it appears in various contexts—in quantum communication [42], thermometry protocols [43], qubit calibration, quantum engines and batteries [44], and on-demand single-photon sources [45,46]. For example, calibration of a large number of qubits in a superconducting quantum processor is a time-costly process, and it has to be done frequently due to uncontrolled frequency drifts of the qubits as well as amplitude and phase drifts of the control electronics. Moreover, in many-qubit systems parasitic ZZ couplings between nearby qubits may lead to fluctuations of qubit transition frequencies. Therefore, having resilience to small drifts in the system and/or in the control parameters is highly beneficial for suppressing the errors due to spectator qubits.

Second, the single-qubit gates with phase-modulated pulses have straightforward usage in gate based quantum computing, where the robustness can mitigate fluctuations of control parameters, *e.g.* over long time scales. Previous works on gates induced by Landau-Zener transitions have employed flux modulation of small-gap composite qubits [47] and modulation by electric pulses in double quantum dots [48,49]. These methods are broadband, therefore scalability is challenging. In contrast, our control method has a modulation bandwidth of only a few MHz, making it suitable for operation in the spectrally crowded environments expected for quantum processors.

Other applications could be in NMR or systems with global control [50], where the same drive pulse acts on more than one site: the amplitude robustness would ensure a homogeneous drive even with variations in the drive-atom coupling strength. Finally, these techniques can be generalized to two-qubit population transfer and gates; of particular relevance is the widely used cross-resonant gate [51–54] for fixed-frequency transmons, where the coupling is realized by near-resonant driving

fields. By applying a similar methodology as the one demonstrated here, the phases of these fields could be modulated in order to achieve the desired two-qubit operation.

The paper is organized as follows. In Sec. II, we introduce the key concepts underlining the experiments. The transfer is addressed in Sec. III, while a general rotation is designed and implemented in Sec. IV. We recapitulate the main findings of the paper in Sec. V.

II. METHODS OF PHASE-MODULATION CONTROL

The Hamiltonian of a qubit with energy level separation $\hbar\omega_{01}$, subjected to a driving field with (time-dependent) angular frequency $\omega_d(t)$ and Rabi amplitude $\Omega(t)$ reads $H = (\hbar\omega_{01}/2)\sigma_z + \hbar\Omega(t)\cos(\omega_d(t)t)\sigma_x$. We perform a frame-rotation $F = \exp(-i\omega_d(t)t\sigma_z/2)$ to a frame corotating with the drive around the z axis, transforming the Hamiltonian as $H \rightarrow FHF^\dagger - i\hbar F(\partial F^\dagger/\partial t)$. With the subsequent use of the rotating wave approximation, we obtain

$$H = \frac{\hbar}{2} \begin{pmatrix} -\Delta(t) & \Omega(t) \\ \Omega(t) & \Delta(t) \end{pmatrix}, \quad (1)$$

where $\Delta(t)$ is the *instantaneous* detuning between the qubit frequency ω_{01} and the drive frequency $\Delta(t) = \omega_d(t) - \omega_{01} + t\partial\omega_d(t)/\partial t$. Here we take the Rabi coupling to be real, without loss of generality, as any phase modulation can be rewritten in terms of a frequency modulation though the choice of the rotating frame. The control parameters of the drive are now the time-dependent Rabi frequency $\Omega(t)$ and the detuning $\Delta(t)$.

The qubit used in our experiments is a transmon device, which can be regarded as an anharmonic oscillator with transitions ω_{01} , ω_{12} , etc. The anharmonicity is provided by the charging energy of the shunting capacitor: $\hbar\omega_{01} - \hbar\omega_{12} = E_C$, $E_C/\hbar \approx 2\pi \times 340$ MHz. The first two levels, with transition frequency $\omega_{01} = 2\pi \times 7.27$ GHz, are used as a qubit. The measured relaxation and decoherence times for this sample were obtained as $T_1 \approx 7$ μ s, $T_2^{\text{Ramsey}} \approx 5$ μ s. The sample was thermally anchored to the mixing chamber of a dilution refrigerator with 10 mK base temperature and connected to room-temperature microwave electronics using ≈ 70 dB of attenuation on the control and ≈ 90 dB of attenuation on the readout lines.

Our control scheme requires modulating the frequency of the pulses, which can be done in a straightforward way by mixing a local oscillator (LO) tone with a modulated intermediate-frequency (IF) signal generated by an arbitrary waveform generator (AWG). We use a typical IQ mixer setup employing a Marki IQ-4509 mixer, with the intermediate frequency signals being generated by a Tektronix 5204 AWG (sampling rate 5 GS/s, bandwidth ≈ 2 GHz) or by a Quantum Machines OPX+ system (sampling rate 1 GS/s, bandwidth ≈ 350 MHz). With this setup it is straightforward to generate a signal with a time-dependent amplitude $\Omega(t)$ and frequency $\omega_d(t)$. Starting with a local oscillator $\text{LO}(t) = \exp(i\omega_{\text{LO}}t)$ and setting $I(t) + iQ(t) \propto \exp(i\omega_{\text{IF}}t)$, one ends up with a signal $\text{RF}(t) = \exp[i(\omega_{\text{LO}} + \omega_{\text{IF}})t]$. Therefore, if the intermediate-frequency signal is $I(t) + iQ(t) = \Omega(t)\exp[i(\omega_d(t) - \omega_{\text{LO}})t]$ a signal $\text{RF}(t) = \Omega(t)\exp[i\omega_d(t)t]$ will be generated with the

desired envelope $\Omega(t)$. In this way, any $\Delta(t)$ can be generated by an appropriate choice of $\omega_d(t)$.

With some desired operation U_{target} in mind, the pulse parameters were optimized such that the cost function $\|U_{\text{realized}} - U_{\text{target}}\|_{\text{Fb}}$ is minimized, where $\|M\|_{\text{Fb}} = \sqrt{\sum_{i,j=1}^2 |m_{ij}|^2} = \sqrt{\text{Tr}(M^\dagger M)}$ is the Frobenius norm. While the full form is necessary for an arbitrary operation, for a population transfer it is sufficient to have the matrix element $U_{10} = \langle 1|U_{\text{realized}}|0\rangle$ satisfy $|U_{10}| = 1$, which is experimentally directly accessible by applying the pulse to a qubit initialized in the ground state and measuring the population of the excited one.

The readout is performed dispersively, using a highly detuned superconducting resonator coupled to the qubit, in the averaged regime. After postprocessing of the acquired data, we obtain a readout noise of $\sigma(P_1) \approx 0.3\%$. Another source of errors is the finite duration of the calibration pulses, which inevitably incorporates the effect of decoherence in the results.

In order to fully characterize the quantum gates, we perform quantum process tomography (QPT) following the standard procedure [55]: the qubit is initialized in the states $|0\rangle$, $|1\rangle$, $(|0\rangle + |1\rangle)/\sqrt{2}$, and $(|0\rangle + i|1\rangle)/\sqrt{2}$, after which it evolves under the driving of the microwave pulse which is studied. Quantum state tomography of the respective final states is then performed in each case using three operations: identity (\mathbb{I}), $(\pi/2)_y$, and $(\pi/2)_x$ rotations, giving rise to the expectation values of the Pauli operators σ_z , σ_x , and σ_y respectively. These experimental results are then used to reconstruct the χ_{exp} process matrix [55], subject to positivity constraints for both the experimental density matrices as well as the reconstructed process matrix. Finally, the fidelity of the quantum gate is characterized by $F(\chi_{\text{exp}}, \chi_{\text{th}}) = \text{Tr}(\chi_{\text{exp}} \cdot \chi_{\text{th}})$, which corresponds to the average gate fidelity [56], where χ_{th} is the theoretically expected process matrix.

Using this approach we realized two fundamental operations: population transfer and arbitrary rotations. First, we explore control schemes leading to a *population transfer* of the qubit from the ground to the excited state. Second, we demonstrate how a similar modulation scheme can be used to implement *amplitude-robust* arbitrary X/Y rotations on the Bloch sphere.

III. ROBUST POPULATION TRANSFER

The standard way of realizing population transfer is by a simple Rabi π pulse; however, Rabi pulses are sensitive to errors both in amplitude and frequency. To find a robust pulse, we start our construction with the observation that ideal adiabatic processes are immune to variations in the path of the control parameters. Indeed, the instantaneous eigenenergies of the Hamiltonian (1) are $E_{\pm}(t) = \pm\hbar\sqrt{\Omega(t)^2 + \Delta(t)^2}/2$, corresponding to the eigenstates $|E_-(t)\rangle = \cos[\Theta(t)]|0\rangle - \sin[\Theta(t)]|1\rangle$ and $|E_+(t)\rangle = \sin[\Theta(t)]|0\rangle + \cos[\Theta(t)]|1\rangle$, where the mixing angle $\Theta(t)$ is defined as $\tan[\Theta(t)] = (\Delta(t) + \sqrt{\Omega(t)^2 + \Delta(t)^2})/\Omega(t)$ and $|0\rangle = (0, 1)^T$ and $|1\rangle = (1, 0)^T$ are the ground and the excited states. We search for a process of duration T , starting at $-T/2$ and ending at $T/2$. Suppose that at $t = \pm T/2$ we have $|\Delta(\pm T/2)| \gg \Omega(\pm T/2)$ and also that $\Delta(t)$ changes sign

(negative at $-T/2$ and positive at $T/2$). Then, at the beginning of the process the mixing angle is zero $\Theta(-T/2) = 0$, and the lower instantaneous eigenstate $|E_-\rangle$ of the Hamiltonian (1) coincides with the ground state $|0\rangle$ of the qubit. At the end of the process, the mixing angle is $\Theta(T/2) = \pi/2$ and the lower eigenstate corresponds, up to a sign, to the excited state $|1\rangle$ of the qubit. For an appropriate choice of parameters, the qubit will adiabatically follow the lower eigenstate, resulting in population transfer.

In practice however, the transfer time T is inevitably finite—which strictly speaking breaks the adiabaticity—and, moreover, a specific choice of trajectory in the parameter space has to be made. While more involved modulation schemes (see, e.g., Ref. [57]) exist, the simplest such choice is a linear chirp of frequency, which requires only one control parameter (the speed of the chirp). This has experimental advantages (easiness of programming the waveform) as well as theoretical ones—since it implements the celebrated Landau-Zener-Stückelberg-Majorana (LZSM) model, which can be solved analytically [58]. We note that early theoretical works [59] proposed to use ac-Stark shifts to modulate the phase appropriately. In the present experiment, we realize this task by implementing the phase modulation directly, leveraging on the mixing methods described in the previous section. In contrast to the present work, the observation of LZSM in circuit QED typically involves direct modulation of the qubit frequency using a strong rf field [60–62].

We parametrize the detuning as

$$\Delta(t) = \Delta_{\text{max}} \frac{2t}{T}, \quad (2)$$

where Δ_{max} is the modulation depth and T is the pulse duration, resulting from the drive frequency modulation $\omega_d(t) = \omega_{01} + \Delta_{\text{max}}t/T + \delta$ and $t \in [-T/2, T/2]$. Note that the additional factor of 2 appearing in the modulation of Δ in Eq. (2) is a result of the definition of the instantaneous detuning. δ is the detuning between the qubit transition frequency ω_{01} and the central/average pulse frequency $\langle \omega_d \rangle_T$, which reduces to the frequency error in the nonmodulated case. If $\delta = 0$, the crossover happens at $t = 0$, when the pulse is resonant with the qubit, with a gap of $\Omega(t = 0)$ in the spectrum. For such a parametrization, it is natural to measure the Rabi frequency Ω and the modulation depth Δ_{max} in units of $\Omega_{2\pi} = 2\pi/T$, the Rabi frequency needed for a 2π rotation without detuning, as the frequency scale is set by T^{-1} .

We start the design of the phase-modulated pulse by studying first a rectangular-shape pulse, see Appendix A. This already results in robustness with respect to the pulse amplitude. To achieve robustness also with respect to detuning, we show that it is sufficient to “soften” the edges of the pulse by using a super-Gaussian shape. This shape reduces the nonadiabatic excitations and, simultaneously, allows the pulse to still be confined in the time-domain (thus avoiding the effect of decoherence). The concept is similar to the rapid adiabatic passage process [63–65], where the shape of the pulse envelope is identified by conditions that achieve the suppression of nonadiabatic excitations. For example, a simple idea is to just eliminate the transition points by imposing that the gap between the instantaneous eigenstates remains constant [66,67].

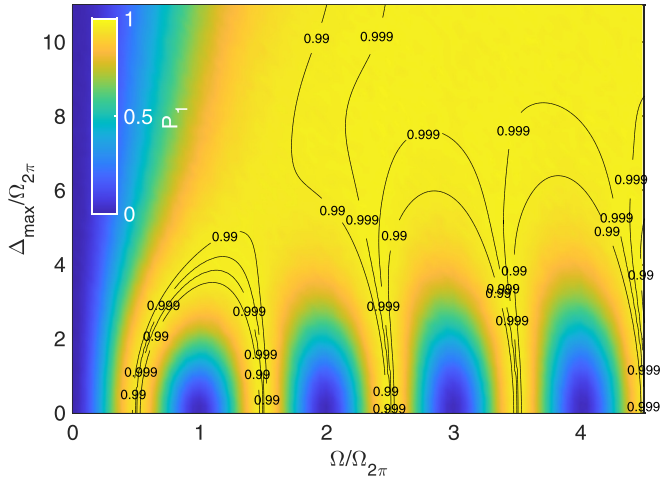


FIG. 1. The experimentally observed population of $|1\rangle$, P_1 , after applying the (Ω, Δ_{\max}) pulse with a super-Gaussian envelope (colored plot), along with the theoretical prediction (contour lines).

Here we adopt a similar strategy, identifying the transitions at the beginning and end of the pulse, and suppressing them by a suitable choice smoothing the pulse edges that keeps the transition rate below a certain threshold. To achieve this, we opted for the super-Gaussian envelope, given by $\Omega(t) = \Omega_0 \exp[-\beta(2t/T)^4]$, with β chosen such that $\Omega(t = \pm T/2) = 0.01\Omega_0$. This choice meets the condition of an *approximately* vanishing amplitude at $t = \pm T/2$, and has an under-the-curve area of $\approx 60\%$ compared to a rectangular pulse of the same duration, resulting in only a moderate increase of the peak amplitude Ω_0 needed for the same rotation. Moreover, it has been shown that Gaussian shapes are effective in reducing the leakage outside the computational space, even leading to less errors than some composite pulses [68]. For such an envelope, we take the pulse amplitude as its average value, such that we get a 2π rotation for $\Omega = \Omega_{2\pi}$ and $\Delta_{\max} = 0$.

The (Ω, Δ_{\max}) parameter space was explored numerically, as well as experimentally. The pulse duration was $T = 200$ ns, corresponding to a 2π Rabi frequency of $\Omega_{2\pi} = 2\pi \times 5$ MHz. Figure 1 shows the experimentally measured population of the first excited state $|1\rangle$ after applying the pulse to a qubit initialized in the ground state $|0\rangle$: a continuous plateau-like region with $P_1 \approx 1$ appears above $\Delta_{\max} \gtrsim 4\Omega_{2\pi}$ and $\Omega \gtrsim 1.5\Omega_{2\pi}$.

Figure 2 shows experimental and theoretical evidence that such a pulse ($\Delta_{\max} = 10.8\Omega_{2\pi}$) provides *simultaneous* robustness in detuning ($\delta = \omega_{01} - \langle \omega_d \rangle_T$) and in amplitude with a wide margin for error: based on the theory the excited state is prepared with a fidelity $P_1 > 99.9\%$ when $T|\delta| \lesssim 3$ and $\Omega \gtrsim 2.45\Omega_{2\pi}$, which is reproduced experimentally, up to the effects of decoherence and relaxation. For comparison, the same holds true for a nonmodulated π pulse for deviations of less than only $\approx 0.02\Omega_{2\pi}$, in either the amplitude or detuning.

In this regime, it is easy to develop an intuitive understanding of these effects: a small amplitude variation merely changes the on-resonance splitting of the instantaneous eigenstates, with no effect on the initial and final mixing angles. As Δ_{\max} increases, so does the rate of change of the

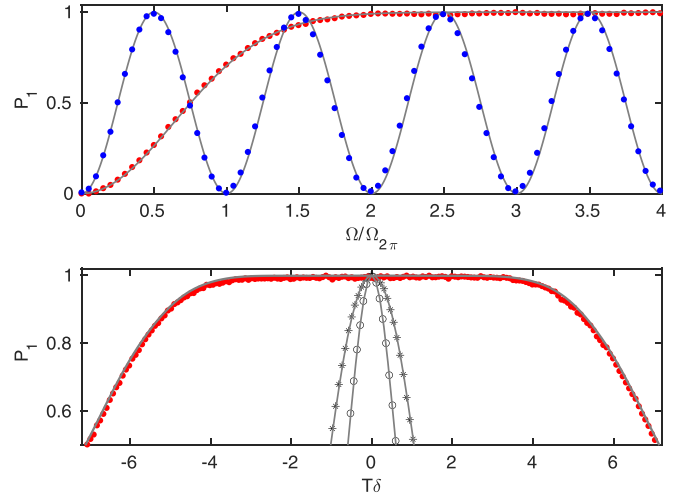


FIG. 2. (Top) The amplitude robustness of the super-Gaussian pulse (red dots), with $\Delta_{\max} = 10.8\Omega_{2\pi}$, compared to the usual non-modulated Rabi pulse (blue dots). (Bottom) The detuning robustness of the super-Gaussian pulse (red dots) with $\Delta_{\max} = 10.8\Omega_{2\pi}$ and $\Omega = 2.5\Omega_{2\pi}$. The gray circles and stars correspond to a Rabi π ($\Omega = \Omega_{2\pi}/2$, $\Delta_{\max} = 0$) and a 3π ($\Omega = 3\Omega_{2\pi}/2$, $\Delta_{\max} = 0$) pulse, respectively. The dots are experimental data, and the solid gray lines on both panels show the theoretical prediction with no fitting parameters.

eigenenergies; then a larger splitting Ω is necessary to avoid the Landau-Zener crossing, which gives rise to the triangular region in the upper left corner of Fig. 1, where the population is not transferred to the excited state. Likewise, a detuning which is small in comparison with Δ_{\max} (which can be made almost arbitrarily large) only shifts the moment at which the pulse is resonant with the qubit. Provided that it happens close to $t = 0$, where $\Omega(t) \approx \Omega_0$, the splitting of the spectrum will be sufficient and will lead to population transfer. Therefore the detuning robustness grows with Δ_{\max} and is approximately Ω -independent (provided that it is sufficiently large).

The approximate adiabaticity of this protocol is demonstrated in Fig. 3: the left panel shows the qubit trajectory (i.e., the components of the density matrix as a function of time) in the frame rotating at its frequency (in which one typically operates) on the Bloch sphere, while the right panel shows the trajectory in the rotating frame as defined above. The difference between the two frames is just a rotation around the z axis by the angle $\int_{-T/2}^t \Delta(\tau) d\tau$, and as $\Delta(t)$ is odd with respect to t they coincide at $t = \pm T/2$. The realized trajectory is close to the adiabatic one, the most prominent difference being a small nonzero y component of the density matrix.

More detailed numerical analyses of the robustness and the adiabaticity of the protocol are given in Appendixes B and C, respectively. Appendix B also discusses the effects of the presence of the second excited state: this places a practical limit on the pulse duration T and Δ_{\max} . For realistic parameters, as the ones presented above, the cross-coupling effects are negligible. This is demonstrated in Fig. 4: even with the large bandwidth of the pulse it is possible to selectively drive the transition between the ground and the first excited state, provided that the modulation depth Δ_{\max} is smaller than the separation between the resonant frequency and

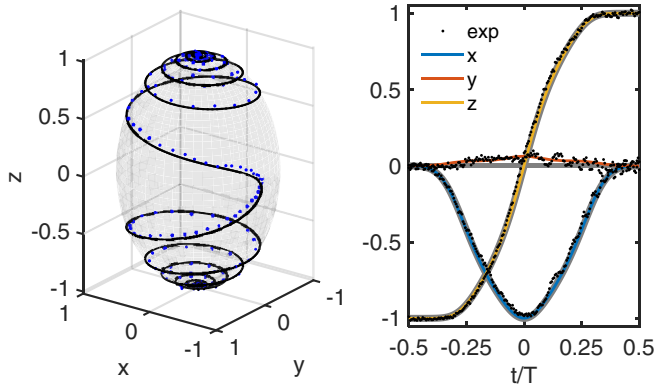


FIG. 3. (Left) Measured trajectory (dots) in the frame rotating at the qubit frequency, along with a theoretical model (solid line). (Right) Trajectory in the frame corotating with the pulse. The theory is given by the solid colored lines, the adiabatic trajectory by the solid gray lines, while the experimental data are shown as dots. The pulse parameters were $\Omega = 8\Omega_{2\pi}$, $\Delta_{\max} = 40\Omega_{2\pi}$ and the pulse duration was $T = 400$ ns.

the two-photon transition frequency $\omega_{02} = (\omega_{01} + \omega_{12})/2 \approx \omega_{01} - E_C/2\hbar$.

IV. ARBITRARY X/Y BLOCH SPHERE ROTATIONS

While the previous pulses enable robust population transfer between the ground and the excited state, they are not general π rotations: nothing guarantees that the resulting unitary transformation U has the proper phase factors—the state transfer experiment only demonstrates that $|U_{10}|^2 \approx 1$. These pulses can be further characterized by performing quantum process tomography: for a unitary propagator $U = c_I I - i \sum_{j=\{X,Y,Z\}} c_j \sigma_j$ ($c_i \in \mathbb{R}$, with $\sum_{j=\{I,X,Y,Z\}} c_j^2 = 1$), the

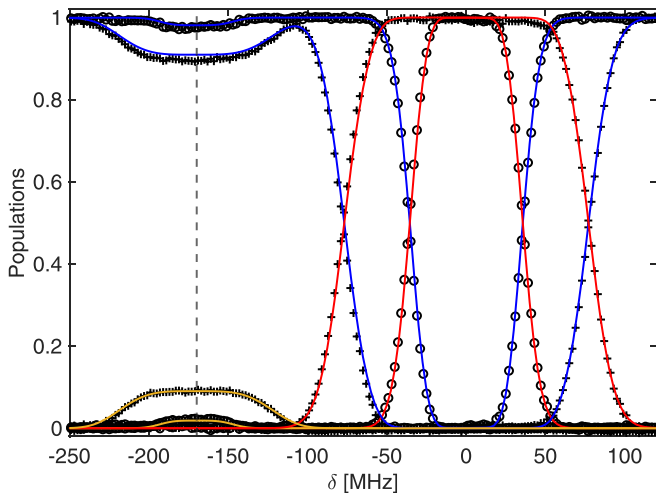


FIG. 4. Theoretically predicted populations of the ground (blue), first (red), and second (yellow) excited states as a function of detuning with respect to the qubit frequency ($\delta = 0$). The circles are experimental data for $\Omega = 2.5\Omega_{2\pi}$ and $\Delta_{\max} = 10.8\Omega_{2\pi}$ and the crosses for $\Omega = 4.5\Omega_{2\pi}$ and $\Delta_{\max} = 21.6\Omega_{2\pi}$. The pulse duration was $T = 200$ ns. The vertical dashed line marks the $2\pi\delta = -E_C/2\hbar$ detuning from the qubit frequency.

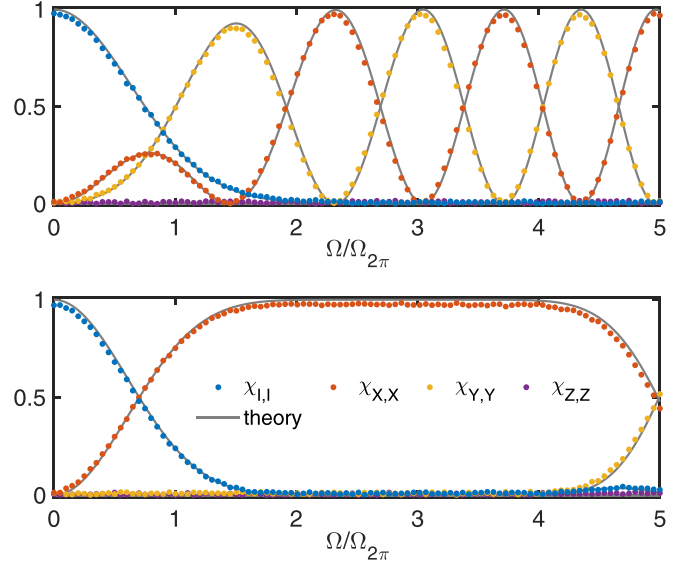


FIG. 5. The diagonal elements of the process matrix χ for the super-Gaussian population transfer pulse (top) and the robust π gate (bottom) as a function of the pulse amplitude Ω . The solid lines show the theoretical prediction while the dots correspond to the experimental χ reconstruction.

elements of the standard process matrix χ correspond to $\chi_{ii} = |c_i|^2$. For a π rotation, one has $c_I = 0$ ($\chi_{I,I} = 0$), and if the rotation is in the vertical plane (i.e., the pulse is resonant with the transition) $c_Z = 0$ ($\chi_{Z,Z} = 0$), while $|c_X|^2 + |c_Y|^2 = 1$. If the π rotation is generated solely by σ_X then $|c_X|^2 = \chi_{X,X} = 1$.

The top panel of Fig. 5 shows the results of QPT for the population transfer pulse, as a function of the pulse amplitude Ω . Above $\Omega \approx 2\Omega_{2\pi}$, as $\chi_{I,I} \approx 0$, it is indeed a π rotation. However, the plane of rotation, while vertical ($\chi_{Z,Z} \approx 0$), is amplitude dependent, as evidenced by the $\chi_{X,X}$ and $\chi_{Y,Y}$ components.

To obtain a robust set of arbitrary angle X/Y rotations we undertake an alternative approach. A target unitary transformation U_{target} is specified, through the rotation angles θ and ϕ on the Bloch sphere: $\mathcal{R}_n(\theta) \equiv \mathcal{R}_\phi(\theta) = \exp(-i\theta\sigma_n/2)$, where $\sigma_n = \cos(\phi)\sigma_x + \sin(\phi)\sigma_y$ is the generator of rotation around the axis $n = (\cos(\phi), \sin(\phi))$ laying in the xOy plane. As the angle ϕ is experimentally controlled by the phase of the drive pulse, and a precise calibration of the qubit frequency is required to avoid unwanted z rotations, we focus on robustness in the amplitude Ω .

We parametrize the pulses by their optimal amplitude Ω_0 (with a rectangular envelope), as well as the time-dependent frequency $\omega_d(t)$. With a pulse duration T , the drive frequency is parametrized as $\omega_d(t) = \omega_{01} + \sum_{k \in \mathbb{N}} a_k \sin(2\pi kt/T)$, in a way similar to Ref. [69], or equivalently:

$$\Delta(t) = \sum_{k \in \mathbb{N}} a_k \left[\sin(kt) + \frac{2\pi kt}{T} \cos(kt) \right], \quad (3)$$

with the Fourier coefficients a_k as free parameters. In contrast to the population transfer, here the phase difference between the qubit frame and the pulse frame needs to be considered, as it effectively sets the phase of the rotation pulse. As was shown in the previous section, by restricting the detuning to

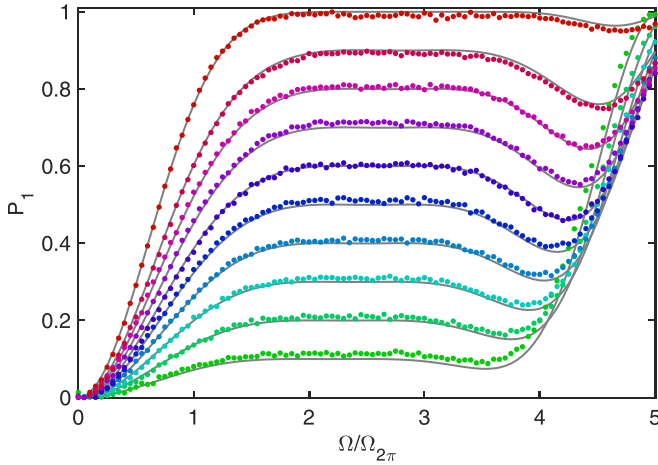


FIG. 6. The experimentally measured population P_1 of the excited state (colored dots) after applying the pulses designed to obtain $P_1 = \{0.1, 0.2, \dots, 1\}$. The solid gray lines show the theoretical prediction with no fitting parameters.

be an odd function of time this difference vanishes, hence no $\cos(kt)$ terms appear in the expansion. The evolution generated by Eq. (3) is fundamentally different from the linearly chirped adiabatic trajectories studied in Sec. III; this is formally shown in Appendix D 4.

The Fourier coefficients a_k , as well as the optimal amplitude Ω_0 , were then numerically optimized using standard gradient descent techniques, such that the resulting pulse is an amplitude robust pulse, i.e., it minimizes the average Frobenius norm $\langle \|U_{\text{target}} - U(\Omega, \Delta)\|_{\text{Fb}} \rangle_{\Omega}$ for Ω close to Ω_0 .

A π pulse generated by σ_x was obtained in this manner, and it was subsequently studied using quantum process tomography. Diagonal terms of the process matrix, corresponding to the decomposition of the propagator in the Pauli basis, are shown in the lower panel of Fig. 5. The resulting profiles clearly exhibit amplitude robustness, but unlike the population-transfer pulse the plane of rotation is constant (here YZ plane) with $\chi_{X,X} \approx 1$ and $\chi_{I,I}, \chi_{Y,Y}, \chi_{Z,Z} \approx 0$.

Pulse parameters that implement rotations for different θ 's can be found by this method: Fig. 6 shows a series of amplitude robust pulses engineered such that $P_1 = [\sin(\theta/2)]^2$; for a qubit initialized in $|0\rangle$, the values are linearly spaced from 1 to 0.1. For all angles, we observe a flat, plateau-like region, for which the desired θ rotation is implemented. Figure 7 shows the corresponding pulses, as well as their parameters. Moreover, the control parameter values are a smooth function of θ , allowing for an arbitrary angle rotation by interpolation of the parameter values (demonstrated in Appendix D 1). Even though robustness against frequency errors was not an optimization goal for these pulses they also offer better performance in this regard compared to the usual Rabi pulses, see Appendix D 2.

In order to study the efficacy and robustness against amplitude variations, we perform QPT for amplitudes $\Omega \in [0, 5\Omega_{2\pi}]$, and quantify the fidelity of these gates as $F(\chi_{\text{exp}}, \chi_{\text{th}}) = \text{Tr}(\chi_{\text{exp}} \cdot \chi_{\text{th}})$, where χ_{th} is the process matrix for the desired operation and χ_{exp} the experimentally reconstructed process matrix. Figure 8 shows the variation of the fidelity versus the Rabi coupling for two arbitrarily chosen

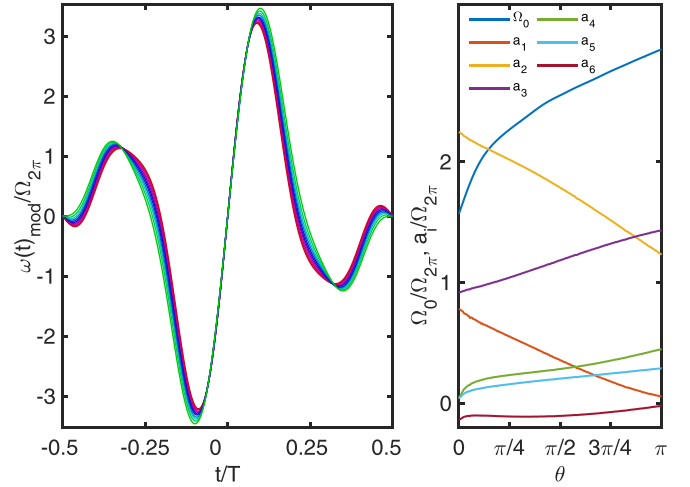


FIG. 7. (Left) Detuning necessary to realize the pulses shown in Fig. 6 (the traces are color-matched). (Right) Pulse parameters, as defined in the text, as a function of the rotation angle.

(θ, ϕ) angles: the fidelity stays high (≈ 0.98) for a wide enough range of amplitudes, while it is theoretically expected to reach $\approx 1-10^{-6}$. This flat region of high fidelity corresponds to the flat region of the populations, shown in Fig. 6. Experimentally reconstructed process matrices at the center of the plateau, also shown in Fig. 8, are in close agreement with the theoretically expected ones.

Further, to characterize the overall performance of these amplitude-robust pulses, we additionally performed randomized benchmarking. This also allows us to demonstrate that the limiting factor for the experimentally observed fidelity is related to the sample and not to the pulses themselves.

We consider the following sequence of operations consisting of $N+2$ gates given by $S = \mathcal{R}_{\pi/2+\phi_R}(-\pi/2)\mathcal{R}_{\phi_R}(\theta_N)\dots\mathcal{R}_{\phi_R}(\theta_1)\mathcal{R}_{\pi/2+\phi_R}(\pi/2)$, where the axis of rotation, set by $\phi_R \in [-\pi/2, \pi/2]$, is chosen randomly and θ_i 's ($i \in [1, N]$) are randomly chosen angles of rotation. This way the whole sequence is effectively a diagonal operator, which corresponds to a rotation generated by σ_z . Therefore, for a qubit initialized in the ground state, we should ideally have $|\langle 0|S|0\rangle|^2 = 1$.

However, in reality, decoherence and errors in the gate implementation will lead to a finite population of the excited state, which will tend to 0.5 with an increasing number of operations (i.e., the qubit will end up in a maximally mixed state). Therefore we take the population of the ground state as a measure of the overall circuit fidelity.

The experimentally obtained curve, demonstrating exponentially decaying fidelity with increasing number of gates, is shown in panel (c) of Fig. 8: the loss per gate is found to be 2.87%. For comparison we performed the same procedure with standard (nonmodulated) Rabi pulses, obtaining the same $\approx 3\%$ error per gate, set by the pulse duration (here $T = 120$ ns) and the relatively short coherence times. Note however that these Rabi pulses have to be very well calibrated and they do not have the robustness property with respect to amplitude [shown in panels (a) and (b) of Fig. 8] of phase-modulated pulses.

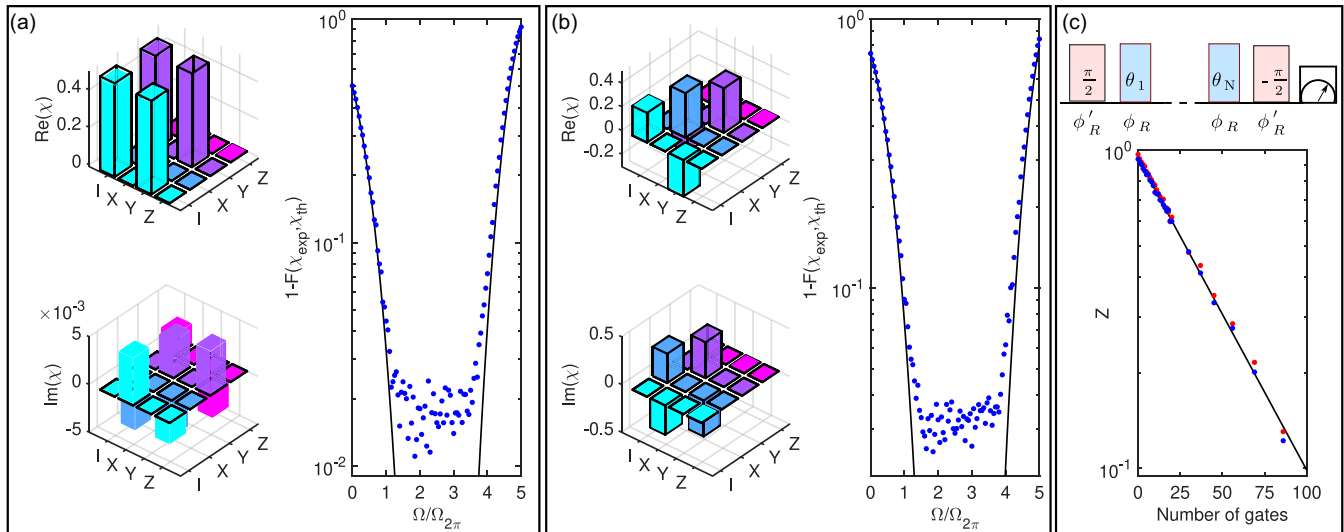


FIG. 8. (a) Real $\text{Re}(\chi)$ and imaginary $\text{Im}(\chi)$ parts of the process matrix for a $\mathcal{R}_{\phi=0}(\theta = \pi/2)$ rotation are shown in a cityscape representation, alongside with the variation of fidelity between the theoretical and experimental process matrices for different values of the Rabi coupling (same horizontal scale as that of Fig. 6). (b) Real $\text{Re}(\chi)$ and imaginary $\text{Im}(\chi)$ parts of the process matrix for an arbitrary x, y -rotation $\mathcal{R}_n(\theta)$ of a single qubit, initialized in state $|0\rangle$ are shown in a cityscape representation. The angle of rotation, $\theta = 2\pi/3$, is chosen arbitrarily (and corresponds to $P_1 = 0.75$) and the axis of rotation is taken at an angle $\phi = 3\pi/4$ with respect to the x axis, where the generator of the rotation is $\sigma_n = \cos(\phi)\sigma_x + \sin(\phi)\sigma_y$. The variation of fidelity between the theoretical and experimental process matrices is shown to the right. In both cases, experimental process matrices correspond to the center of the respective flat regions. The experimentally obtained elements of the process matrices are shown with colored opaque bars, while the black wire-frame bars correspond to the theoretically expected process matrices. (c) Top: the pulse sequence for the randomized benchmarking, where $\phi'_R = \phi_R + \pi/2$. Bottom: experimental results from randomized benchmarking of the amplitude-robust quantum gates (blue dots), compared to the normal Rabi pulses of the same duration (red dots), along with an exponential decay fit (solid black line).

Therefore, even higher fidelities can be achieved in principle with higher-quality samples, where the errors due to instrumentation and calibration start to be comparable with those resulting from decoherence.

V. DISCUSSION AND CONCLUSIONS

For the success of the quantum-computing research programme with superconducting qubits, reducing the sensitivity to imperfections and noise is of utmost importance. With gradual improvements in the decoherence times over the last years, errors in amplitude and frequency of the pulses used to manipulate these systems become the dominant source of fidelity loss.

Here we have proposed theoretically and realized experimentally control protocols for robust qubit state manipulation employing phase-modulated pulses. The control waveforms used here are stable—meaning that errors in the operations do not increase rapidly under small perturbations of the control parameters. The number of optimization parameters is not very large, which makes the numerical optimization less time consuming.

In the first part, we demonstrated that a simple scheme, based on a Landau-Zener-like process, can result in an operation that realizes population transfer between two levels with considerable robustness: any amplitude above a threshold value leads to a complete population transfer, while the frequency of the pulse can be detuned by several tens of MHz from the transition frequency. In the second part, we presented a set of pulses which realize amplitude-robust X/Y

rotations. The performance of these pulses was evaluated using quantum process tomography as well as randomized benchmarking, showing that they realize the desired operation with high fidelity. Furthermore, it should be possible to generalize this approach for multistate (e.g., qutrit) and multiqubit control. Consider for example two flux-tunable qubits that can be brought in the avoided-crossover region by rapid flux excursions. In this case, a Landau-Zener-like process can be implemented between the states $|10\rangle$ and $|01\rangle$, thus implementing an iSWAP gate. Another situation is the cross-resonant gate, where two fixed-frequency qubits are coupled with a constant coupling strength and they are driven by microwave fields. In this case, in a rotating frame similar to that used throughout this paper, the eigenenergies can be modulated by detunings and the qubits can be brought into the crossover region where they exchange energy.

In our measurements, we also found that the comparatively small bandwidth of the arbitrary waveform generator did not greatly affect the performance of the pulses, hence our control scheme can be implemented with regular instruments available in most labs. However, with the relentless advances in the quality of qubits, we expect that eventually the fidelities and gate errors will be limited by technical specifications such as the sampling rate and the characteristics of the mixers—although these also improve continuously due to efforts in microwave engineering. Finally, our methods can be readily applied to any other experimental platform (trapped ions, NV centers, etc.) where a two-level system is manipulated using microwave or laser pulses.

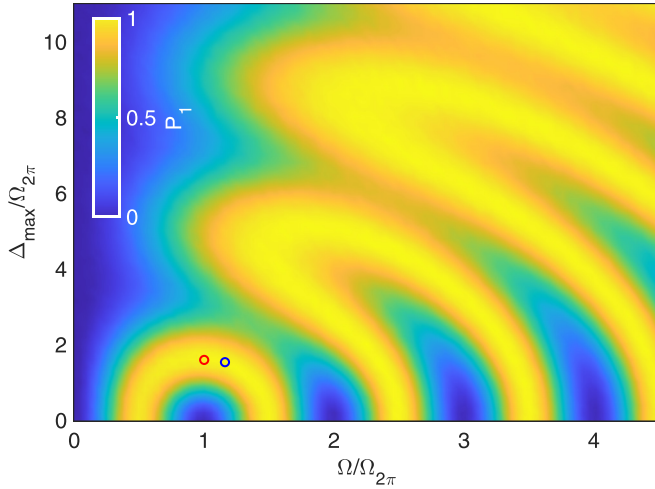


FIG. 9. Experimentally obtained population of $|1\rangle$, P_1 by applying the (Ω, Δ_{\max}) pulse to the qubit initialized in $|0\rangle$. The red and blue circles indicate an amplitude or detuning robust pulse respectively.

ACKNOWLEDGMENTS

We are grateful to Aidar Sultanov for help with the experiments at various stages of this work. This project has received funding from the European Union project OpenSuperQ+. We acknowledge also financial support from Grant No. FQXi-IAF19-06 (“Exploring the fundamental limits set by thermodynamics in the quantum regime”) of the Foundational Questions Institute Fund (FQXi), a donor advised fund of the Silicon Valley Community Foundation. This work was performed as part of the Academy of Finland Centre of Excellence program (Project 352925) and it has used of the experimental facilities of the Low Temperature Laboratory and Micronova of the OtaNano research infrastructure.

APPENDIX A: ROBUST POPULATION TRANSFER WITH CONSTANT AMPLITUDE PULSES

Here we discuss the case of LZMS drive realized with constant amplitude pulses. The scheme is principally the same as the one in the main text, where the detuning $\Delta(t)$ is a linear function, but the pulses are rectangular.

Figure 9 shows the experimentally measured population of the first excited state $|1\rangle$ after applying such a pulse to a qubit initialized in the ground state $|0\rangle$. As opposed to the plateau obtained with super-Gaussian pulses (see Fig. 1), several nonconnected stripes with $P_1 = 1$ are observed for rectangular-envelope pulses, appearing at successively higher Rabi and detuning frequencies. Still, we can identify two points on the first lobe of this pattern, which realize pulses robust to amplitude offsets (red circle in Fig. 9), and to detuning offsets (blue circle in Fig. 9) respectively. While the higher order lobes shown in Fig. 9 can in principle offer greater amplitude/frequency robustness at the expense of a larger Rabi and modulation frequencies, they are not of great interest due to the higher levels of power required.

The top panel of Fig. 10 highlights the amplitude robustness in comparison with a resonant Rabi pulse: theoretically

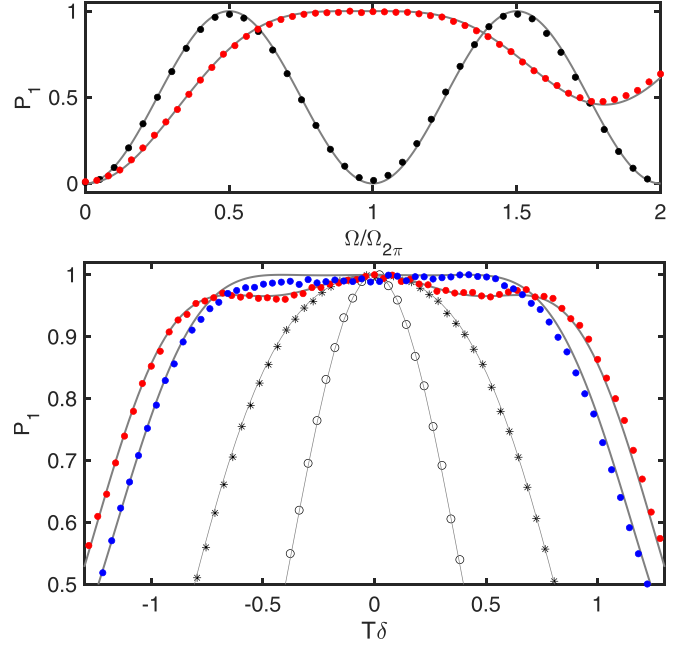


FIG. 10. (Top) The amplitude robust pulse (red circle on Fig. 9, $\Delta_{\max} = 1.64\Omega_{2\pi}$, $\Omega = \Omega_{2\pi}$) compared to the resonant Rabi drive. (Bottom) The detuning robustness of the amplitude robust pulse and the detuning robust one (blue circle in Fig. 9, $\Delta_{\max} = 1.54\Omega_{2\pi}$, $\Omega = 1.16\Omega_{2\pi}$). The gray circles and stars correspond to a Rabi π and a 3π pulses, respectively. The solid gray lines on both panels show theoretical predictions with no fitting parameters.

$P_1 > 99.9\%$ is achieved for the range of amplitudes $\Omega \in [0.82\Omega_{2\pi}, 1.12\Omega_{2\pi}]$, which is reproduced experimentally, up to the effects of decoherence and relaxation. At the same time, this pulse is not robust against detuning from the qubit frequency ($\delta = \omega_{01} - \omega_d$), as shown in in the bottom panel of Fig. 10. A pulse with slightly different parameters (blue circle in Fig. 9), on the other hand, results in a population transfer with $P_1 > 99.9\%$ when it is detuned from the qubit frequency by less than $T\delta \lesssim 0.5$.

The performance of these rectangular pulses is quite similar to those found in Refs. [30,31], as the detuning profile obtained there is almost linear, with the added benefit of a simpler implementation.

Next, we focus on deepening the theoretical understanding of the pattern of fringes observed experimentally.

The Hamiltonian given by Eq. (1) with Ω time-independent has two instantaneous eigenstates $|E_+(t)\rangle$ and $|E_-(t)\rangle$ with energies $E_{\pm}(t) = \pm\hbar\sqrt{\Omega^2 + \Delta(t)^2}/2$. The eigenstates can be parametrized as $|E_-(t)\rangle = (-\sin(\Theta), \cos(\Theta))^T$ and $|E_+(t)\rangle = (\cos(\Theta), \sin(\Theta))^T$, where the mixing angle is given by $\tan[\Theta(t)] = (\Delta(t) + \sqrt{\Omega^2 + \Delta(t)^2})/\Omega$. For $\Delta(t) = 2\Delta_{\max}t/T$, we have $\Delta(\pm T/2) = \mp\Delta_{\max}$, and as a consequence the mixing angles then satisfy $\Theta(-T/2) + \Theta(T/2) = \pi/2$.

If we denote the mixing angle at $t = -T/2$ by Θ_0 , then the eigenstates in the beginning and the end of the process read $|E_-(T/2)\rangle = (-\sin(\Theta_0), \cos(\Theta_0))^T$, $|E_+(-T/2)\rangle = (\cos(\Theta_0), \sin(\Theta_0))^T$, $|E_-(T/2)\rangle = (-\cos(\Theta_0), \sin(\Theta_0))^T$, and $|E_+(T/2)\rangle = (\sin(\Theta_0), \cos(\Theta_0))^T$.

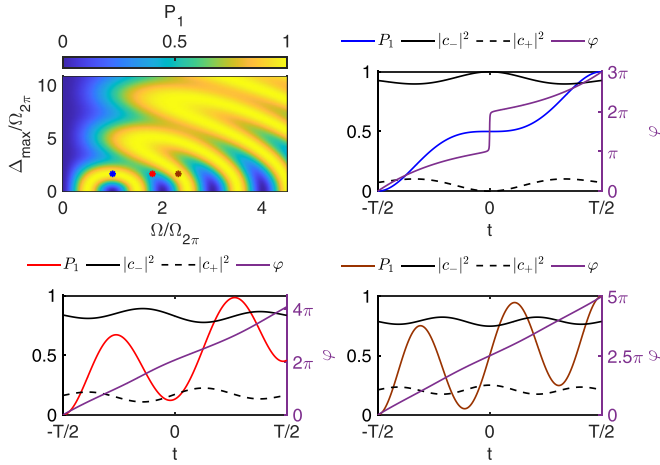


FIG. 11. (Top left) Simulation of the population transfer as a function of Ω and Δ_{\max} . Other panels: the time evolution, given by the population of the excited state P_1 (colored), coefficients $|c_{\pm}|^2$ (black, solid and dashed respectively) and their relative phase φ (purple, right scale) for the three points highlighted in the top-left panel (the colors of the dots and P_1 traces are matched).

Any state $|\psi\rangle$ can be decomposed into $|E_{\pm}(t)\rangle$ as $|\psi\rangle = c_-(t)|E_-(t)\rangle + c_+(t)|E_+(t)\rangle$ and the time evolution is given by the time dependence of $c_{\pm}(t)$. For a qubit initialized in the ground state $|0\rangle = (0, 1)^T$, we have $c_-(-T/2) = \cos(\Theta_0)$ and $c_+(-T/2) = \sin(\Theta_0)$, and Rabi flopping will occur. For an adiabatic trajectory, we have $|c_{\pm}(t)| = \text{const}$, with the state only acquiring a time-dependent phase $c_{\pm}(t) = c_{\pm}(-T/2)e^{\pm i\varphi(t)/2}$, where $\varphi(t) = \int_{-T/2}^t \sqrt{\Omega^2 + \Delta^2(t)} dt$. Only if $\varphi(T/2) = (2k+1)\pi$ ($k \in \mathbb{Z}$) will the qubit end up in the excited state $|1\rangle = (1, 0)^T$.

Even if the trajectory is not adiabatic the same holds true: the final state $|1\rangle$ is obtained only when $|c_{\pm}(-T/2)| = |c_{\pm}(T/2)|$ with a relative phase factor of $e^{i\varphi} = -1$. This condition leads to the interference-like pattern seen in Fig. 9, reproduced here numerically in Fig. 11. The same figure shows several trajectories, for different parameter values, demonstrating this interference effect: in all cases the trajectory is approximately adiabatic ($|c_{\pm}(t)| \approx \text{const}$) and $|c_{\pm}(-T/2)| = |c_{\pm}(T/2)|$ is satisfied, only the accumulated phase φ is different: $\varphi(T/2) = 3\pi$ and $\varphi(T/2) = 5\pi$ leads to $P_1(T/2) = 1$, while for $\varphi(T/2) = 2\pi$, we have $P_1(T/2) \approx 0.5$.

Unlike with a constant amplitude pulse, the super-Gaussian envelope ensures that the mixing angle at $t = \pm T/2$ is ≈ 0 and $\approx \pi/2$, respectively. Therefore there will be no Rabi flopping, and the relative phase of the two eigenstates does not matter, leading to the plateau observed in Fig. 1 of the main text and Fig. 12.

APPENDIX B: ROBUSTNESS OF LINEARLY MODULATED SUPER-GAUSSIAN PULSES

In the rotating wave approximation, the Hamiltonian of a three-level system subject to a drive can be written as

$$H = \hbar \begin{pmatrix} -\Delta_{01}(t) & \Omega_{01}(t)/2 & 0 \\ \Omega_{01}(t)/2 & 0 & \Omega_{12}(t)/2 \\ 0 & \Omega_{12}(t)/2 & \Delta_{12}(t) \end{pmatrix}, \quad (\text{B1})$$

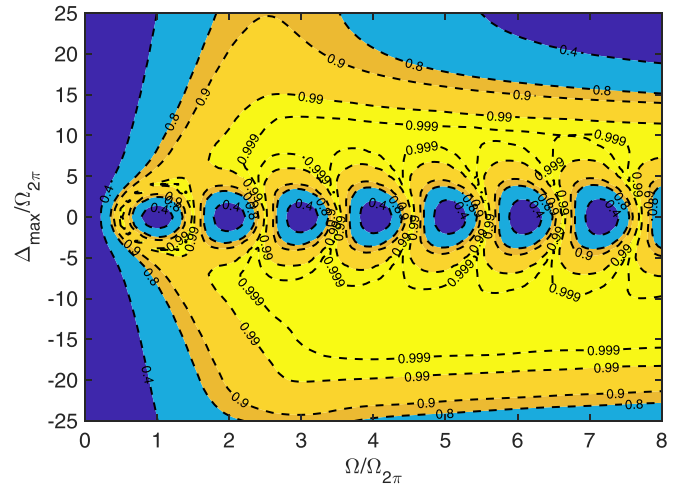


FIG. 12. Contour plot of P_1 as a function of (Ω, Δ_{\max}) with a super-Gaussian envelope, simulated using Eq. (B1).

where Δ_{01} and Δ_{12} are the detunings between the drive frequency and the f_{01} and f_{12} transition frequencies. Ω_{01} and Ω_{12} are the Rabi frequencies that drive the 01 and 12 transitions, differing only by the ratio of the transition dipole moments $\Omega_{12}/\Omega_{01} = g_{12}/g_{01} = \lambda$. We assume that the 02 dipole moment $g_{02} = 0$. The model presented here can reproduce the two-photon (i.e., Raman) transitions as well, and should describe well all of the effects that one typically observes with short duration pulses and/or high amplitudes.

For a transmon, we have $E_J/E_C \rightarrow \infty$ then $\lambda \rightarrow \sqrt{2}$ and $\omega_{12} \approx \omega_{01} - E_C/\hbar$. Here we assume $\lambda = \sqrt{2}$, as it represents the worst-case scenario for the effects of the cross-coupling. We take the experimental value of $E_C/\hbar = 2\pi \times 340$ MHz.

A $T = 60$ ns pulse with a super-Gaussian envelope was simulated using Eq. (B1). Figure 12 shows the population of the first excited state P_1 as a function of (Ω, Δ_{\max}) , and is comparable to Fig. 1 of the main text. While the general structure is the same now it is clear that the protocol breaks down for large values of Δ_{\max} , by driving either the 12 or 02 transitions. The model presented in the main text is invariant under $\Delta_{\max} \rightarrow -\Delta_{\max}$, as it just changes whether the qubit follows the lower or higher eigenstate of the Hamiltonian. Here, however, the presence of the second level breaks this symmetry and gives rise to the behavior seen in Fig. 12.

The detuning robustness can be studied in the same way; (δ, Ω) maps are shown in Fig. 13. The results are in accordance with the statements made about the detuning robustness in the main text: generally it grows with Δ_{\max} and is approximately independent of Ω , above a threshold value. The existence of the second excited state shows up as in Fig. 12: it breaks the $\Delta_{\max} \rightarrow -\Delta_{\max}$ and $\delta \rightarrow -\delta$ symmetries.

For longer pulses ($E_C T/\hbar \ll 1$), the detuning robustness, as well as the pulse bandwidth, is determined primarily by the modulation depth Δ_{\max} : if it is sufficiently smaller than the anharmonicity one is still able to selectively drive the transition from the ground to the first excited state, without populating the second excited state. Figure 4 in the main text demonstrates this theoretically, as well as experimentally: for a $T = 200$ ns pulse one can find parameters (Ω, Δ_{\max}) that robustly drive the transmon to the first excited state; the

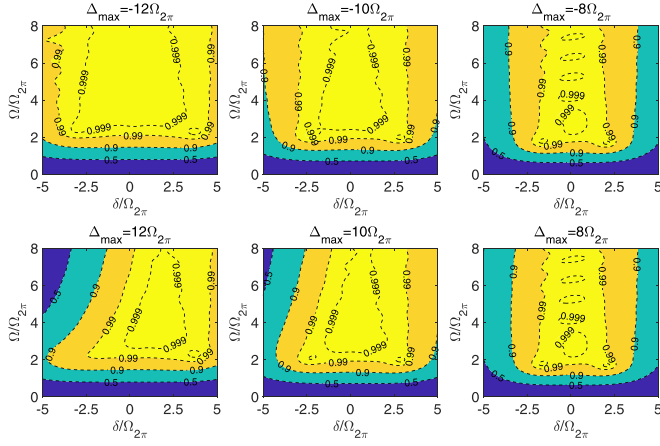


FIG. 13. Contour plot of P_1 , showing the detuning robustness of the protocol as a function of Ω , for several values of Δ_{\max} .

second excited state is only populated if the pulse is detuned by $\delta \approx E_C/2\hbar$.

Overall, one can conclude that for moderate values of Δ_{\max} (i.e., $\Delta_{\max} \ll E_C T/\hbar$) the protocol is unaffected by the existence of the second excited state. Additionally if one considers longer pulse durations higher order states can be disregarded, while still providing a considerable degree of robustness.

APPENDIX C: SUPER-GAUSSIAN VERSUS OTHER ENVELOPES

In the main text several criteria for the envelope were laid out, most important of which is the vanishing amplitude at the end of the pulse. The super-Gaussian envelope was chosen as a balance between the spectral width of the pulse and a lower peak amplitude compared to, e.g., a Gaussian pulse. An added benefit is that the flatness of the envelope near $t = 0$ leads to an increased detuning robustness, which was not extensively studied for other RAP-like pulses. For a pulse detuned by δ from the transition frequency, the eigenenergy spectrum will attain its minimum value at $t = \frac{T\delta}{2\delta_{\max}} \neq 0$.

The rapid-adiabatic-passage family of pulses offers a lot of possibilities, without a clear winner in terms of performance. Many of the used envelopes (e.g., a Gaussian, $\text{sech}(t/\tau, \dots)$) have the same qualitative shape: a peak at $t = 0$ with a relatively rapid drop-off. Here we make a comparison with a Gaussian envelope ($\Omega(t) = \Omega_0 \exp[-\beta(2t/T)^2]$, with $\beta = -\ln(0.01)$, such that $\Omega(t = \pm T/2) = 0.01\Omega_0$), and the findings should carry over to other envelopes.

For a Gaussian envelope, the amplitude will be suppressed more compared to its peak value $\Omega(t = 0)$ than for the super-Gaussian envelope. However, due to the envelope shape the Gaussian pulse has a higher peak amplitude. These are two competing effects, and it is not possible to immediately say which one is dominant. To investigate this, we performed a numerical study of the detuning robustness: Figs. 14 and 15 show that regardless of the amplitude and the modulation depth Δ_{\max} the super-Gaussian pulse offers a higher degree of robustness.

Additionally, one can study the adiabaticity of the pulses according to the criterion $\eta = \frac{\|\dot{\Omega}\Delta - \Omega\dot{\Delta}\|}{(\Omega^2 + \Delta^2)^{3/2}}$, for an adiabatic

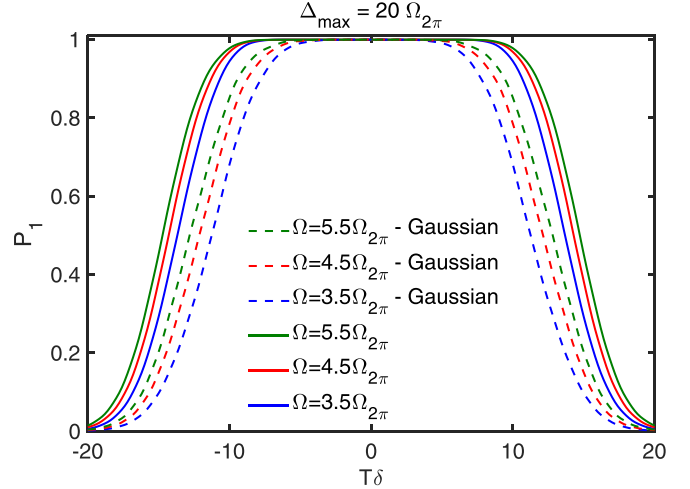


FIG. 14. The detuning robustness of the Gaussian (dashed lines) and super-Gaussian (solid lines) as a function of the pulse amplitude, normalized to the same area-under-the-curve, for $\Delta_{\max} = 20\Omega_{2\pi}$.

trajectory $\eta \ll 1$ [64]. Figure 16 shows the maximum value $\max_t(\eta)$ as a function of (Ω, Δ_{\max}) for the Gaussian and super-Gaussian envelope. The super-Gaussian pulse has a similar average value of η (not shown), but a lower peak value, which implies an adiabatic trajectory, as was claimed in the main text.

More generally, the detuning robustness can be studied as a function of the envelope order n . While the specifics depend on the amplitude Ω and the modulation depth Δ_{\max} , in general a transfer with high efficiency (i.e., $P_1 \approx 1$) is realized for relatively smooth envelopes ($n \lesssim 10$). This can qualitatively be understood in the following way: for large values of n the strength of the drive field changes abruptly close to the pulse edges, leading to a nonadiabatic trajectory. These effects are demonstrated in Fig. 17.

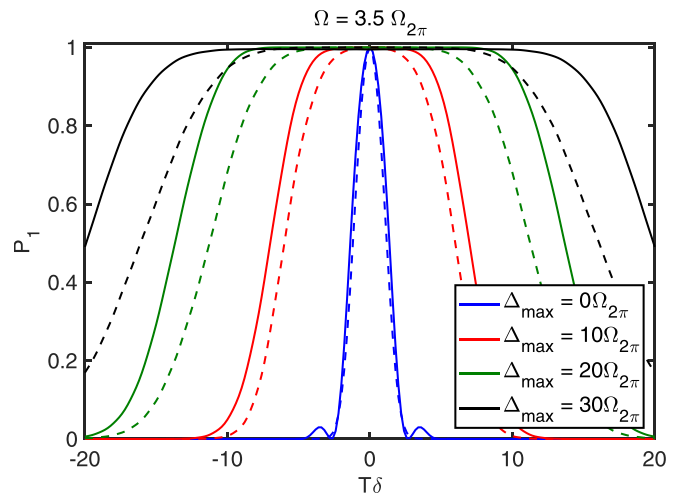


FIG. 15. The detuning robustness of the Gaussian (dashed lines) and super-Gaussian (solid lines) as a function of the modulation depth Δ_{\max} . The envelopes were normalized to the same area, with $\Omega = 3.5\Omega_{2\pi}$.

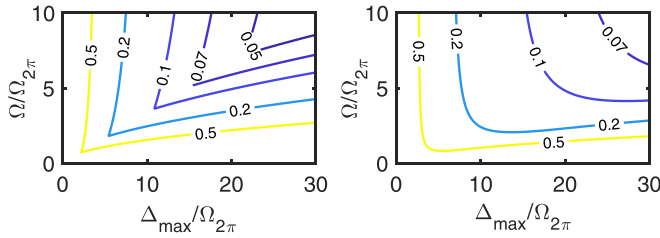


FIG. 16. The maximum value of η for a pulse with a super-Gaussian (left) and a Gaussian envelope (right).

APPENDIX D: ARBITRARY X/Y BLOCH SPHERE ROTATIONS

1. Arbitrary rotations based on the modulated pulses

Without losses, the time evolution operator U fully describes the effect of a gate on a qubit. In order to analyze the gate based on a frequency/phase modulated drive, here it is more convenient to work in the frame corotating with the qubit (and not the pulse, as presented in the main text). Then the Hamiltonian is given by $H = |e\rangle\langle g|\Omega e^{i\Phi(t)} + h.c.$, where $\Phi(t) = (\omega_d(t) - \omega_{01})t$. With the initial condition $U(-T/2) = I$ the equation of motion for $\dot{U} = -iHU$ can be integrated to obtain $U(T/2)$.

Any U can be decomposed into linear combinations of $\sigma_0 = I$, σ_x , σ_y , and σ_z : $U = c_0\sigma_0 - i\sum_{j=1}^3 c_j\sigma_j$. For a rotation by angle θ generated by σ_x , the corresponding evolution operator is given by $U = \begin{pmatrix} \cos(\theta/2) & i\sin(\theta/2) \\ i\sin(\theta/2) & \cos(\theta/2) \end{pmatrix} = \cos(\theta/2)\sigma_0 + i\sin(\theta/2)\sigma_x$. If the plane of rotation is off, i.e., the generator of rotation is a linear combination of σ_x and σ_y , there will be a nonzero σ_y component in U .

The goal of the second part of this work was to create a frequency-modulated pulse which is effectively a rotation generated by σ_x , while simultaneously achieving insensitivity to amplitude deviations.

In the main text, this was demonstrated using quantum process tomography. Here we present a diagram which completely characterizes our pulses as a function of the rotation angle θ and their amplitude Ω . The evolution operator is calculated; Fig. 18 shows the σ_x and σ_y components of U , along with the population of the excited state P_1 , and its deviation from the desired value $P_1(\theta) = [\sin(\theta/2)]^2$. We see that in the amplitude-robust region (i.e. where $P_1 \approx [\sin(\theta/2)]^2$) the

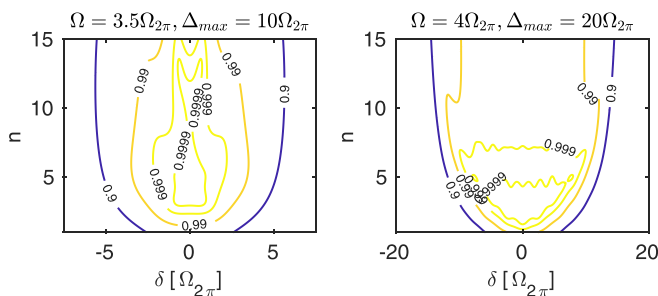


FIG. 17. Contour plot of the excited state probability P_1 , as a function of the detuning δ as well as the pulse envelope order n , for select values of Ω and Δ_{max} .

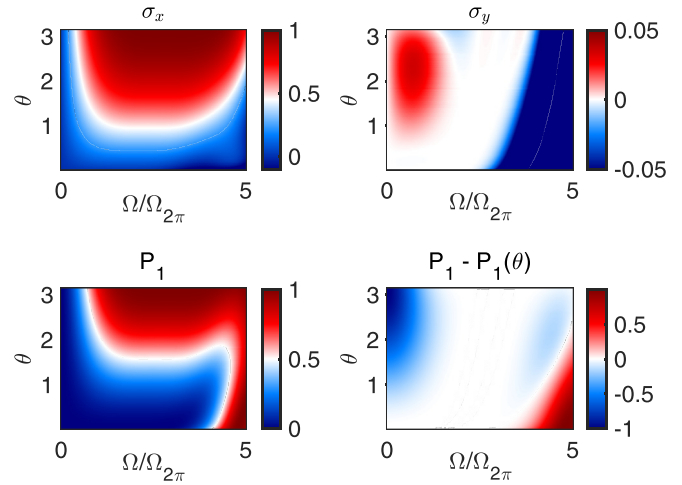


FIG. 18. The σ_x (top left) and σ_y (top-right) components of U , the population of the excited state (bottom left) and the deviation from the desired value $P_1(\theta) = \sin(\theta/2)^2$ (bottom right) as a function of θ and Ω .

σ_y component is negligible and the σ_x component is what generates the rotation. Additionally, this map was computed by interpolating pulse parameters between the ten optimized ones (for $P_i = i/10$, where $i \in 1, \dots, 10$) and shows that an amplitude robust arbitrary rotation can be obtained this way.

2. Detuning robustness of arbitrary rotations

Here we study the effect of finite detuning, i.e., an error in the pulse frequency, of the pulses presented in Sec. IV of the main text. We present the results in the same manner as Fig. 2 of the main text as well as Appendix C. Figure 19 compares the modulated and the usual Rabi pulses for target angles $\theta = \pi$ and $\theta = \pi/2$: although both deviate from the desired value at nonzero detunings, the Rabi ones are more affected by it. It is worth reiterating that detuning robustness was not a design goal for these pulses, as for $\delta \neq 0$ the qubit phase evolves at a rate of δ , and the (vertical) plane of rotation is not easily controllable. Nevertheless, the results presented here show that the modulated pulses are more resilient to frequency errors than the usual Rabi ones.

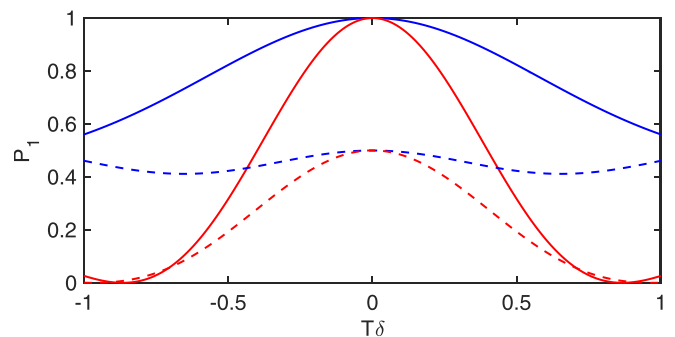


FIG. 19. The population of the excited state after applying the robust (blue) and Rabi (red) $\pi/2$ (dashed line) and π (solid line) pulses, to a qubit initialized in the ground state, as a function of detuning δ .

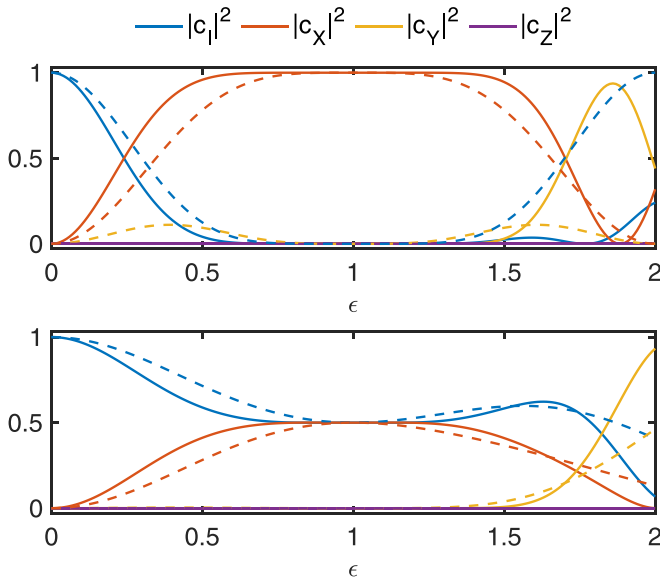


FIG. 20. The expansion of the propagator $U = \sum_i \sigma_i c_i$, $i \in \{I, X, Y, Z\}$ as a function of the relative amplitude $\epsilon = \Omega/\Omega_0$ for our modulated pulse (solid lines) and a three-pulse composite (dashed). Two θ 's are shown: π on the top panel and $\pi/2$ on the bottom one.

3. Comparison with composite pulses

Here we perform a comparison of our pulses to a short composite pulse presented in Ref. [70], engineered to provide amplitude robustness. As the sequence consists of only three consecutive pulses, the total duration of the composite pulse should be comparable to the pulses presented in this work. Figure 20 shows the expansion of the propagator U , in terms of the Pauli matrices, as a function of the relative amplitude $\epsilon = \Omega/\Omega_0$ (Ω_0 is the optimal amplitude). Our pulses outperform the composite one, the working range is wider and flatter. This is especially evident in the case of a $\pi/2$ pulse, where the composite pulse deviates approximately quadratically $(\epsilon - 1)^2$ from the target operation, while the modulated one is plateaulike around $\epsilon = 1$. Longer pulse sequences might offer more robustness, at the expense of a longer duration. Finding such sequences is also not trivial: in the same work [70] it was also shown that the three-pulse sequence outperforms a six-pulse one.

4. Nonequivalence with a linear chirp

The Hamiltonian used for realizing the robust X/Y gate reads $H(t) = \hbar\Delta(t)\sigma_z/2 + \hbar\Omega_0\sigma_x/2$, where $\Delta(t)$ is given by equation Eq. (3) realizes some trajectory $U(t)$ for the evolution operator. The question of interest here is whether there is an alternative parametrization that makes the system evolve along the same trajectory, at a different rate, such that the driving Hamiltonian is a linear chirp. Provided that it exists, such a trajectory can be written as $U(t(\tau))$, where the implicit $t(\tau)$ dependence encodes the mapping. The equation of motion then becomes $dU/d\tau = -iH(\tau)U(\tau)$. On the other hand $dU/d\tau = (dU/dt)(dt/d\tau) = -iH(t(\tau))U(t(\tau))dt/d\tau$. Equating the two and acting with U^\dagger from the right gives $H(\tau) = H(t(\tau))dt/d\tau$.

With the desired form $H(\tau) = \hbar\Omega(\tau)\sigma_x/2 + \hbar\tau\alpha\sigma_z/2$, where $\Omega(\tau)$ is the time-dependent amplitude and α the chirp rate, the previous equation can be solved componentwise. By multiplying both sides by σ_x and taking the trace one gets $\Omega(t) = \Omega_0 dt/d\tau$. Similarly the σ_z component reads $\alpha\tau = \Delta(t)dt/d\tau$, which can be solved by separation of variables. The left-hand side is trivially integrated, while for the right-hand side, one can use integration by parts, along with $\Delta(t) = \omega_d(t) - \omega_{01} + t\partial\omega_d(t)/\partial t$, to obtain $\alpha\tau^2/2 = (\omega_d(t) - \omega_{01})t$ (the integration was performed from 0 to τ on the left-hand side and from 0 to t on the right-hand side along with an implicit change of variables, and the integration constant was set such that $t = 0$ corresponds to $\tau = 0$). If the pulses are to have the same duration, substituting $\tau = t = T/2$ gives α .

For the mapping $t(\tau)$ to be valid, it needs to be a bijection. However, for the form of $\omega_d(t)$ used in Sec. IV, that is not the case: from Fig. 7, one can deduce that $(\omega_d(t) - \omega_{01})t$ is non monotonic and it changes sign, and a valid solution cannot be found. Thus one can conclude that the trajectory realized by such a modulation belongs to a different class of equivalence compared to the ones generated by a linear chirp, with any envelope.

Even if a mapping could be found, nothing guarantees that the resulting pulse would have the same robustness feature, as $H(t(\tau))$ does not commute with the “error” term $\epsilon\sigma_x$ at all times.

- [1] N. Rosen and C. Zener, Double Stern-Gerlach experiment and related collision phenomena, *Phys. Rev.* **40**, 502 (1932).
- [2] M. P. Silveri, J. A. Tuorila, E. V. Thuneberg, and G. S. Paraoanu, Quantum systems under frequency modulation, *Rep. Prog. Phys.* **80**, 056002 (2017).
- [3] K. Temme, S. Bravyi, and J. M. Gambetta, Error mitigation for short-depth quantum circuits, *Phys. Rev. Lett.* **119**, 180509 (2017).
- [4] Y. Li and S. C. Benjamin, Efficient variational quantum simulator incorporating active error minimization, *Phys. Rev. X* **7**, 021050 (2017).
- [5] A. Kandala, K. Temme, A. D. Córcoles, A. Mezzacapo, J. M. Chow, and J. M. Gambetta, Error mitigation extends the

computational reach of a noisy quantum processor, *Nature (London)* **567**, 491 (2019).

- [6] M. Silva, E. Magesan, D. W. Kribs, and J. Emerson, Scalable protocol for identification of correctable codes, *Phys. Rev. A* **78**, 012347 (2008).
- [7] E. Magesan, J. M. Gambetta, and J. Emerson, Characterizing quantum gates via randomized benchmarking, *Phys. Rev. A* **85**, 042311 (2012).
- [8] F. Motzoi, J. M. Gambetta, P. Rebentrost, and F. K. Wilhelm, Simple pulses for elimination of leakage in weakly nonlinear qubits, *Phys. Rev. Lett.* **103**, 110501 (2009).
- [9] J. M. Gambetta, F. Motzoi, S. T. Merkel, and F. K. Wilhelm, Analytic control methods for high-fidelity unitary operations in a weakly nonlinear oscillator, *Phys. Rev. A* **83**, 012308 (2011).

- [10] F. Motzoi and F. K. Wilhelm, Improving frequency selection of driven pulses using derivative-based transition suppression, *Phys. Rev. A* **88**, 062318 (2013).
- [11] J. Bylander, S. Gustavsson, F. Yan, F. Yoshihara, K. Harrabi, G. Fitch, D. G. Cory, Y. Nakamura, J.-S. Tsai, and W. Oliver, Noise spectroscopy through dynamical decoupling with a superconducting flux qubit, *Nat. Phys.* **7**, 565 (2011).
- [12] B. Pokharel, N. Anand, B. Fortman, and D. A. Lidar, Demonstration of fidelity improvement using dynamical decoupling with superconducting qubits, *Phys. Rev. Lett.* **121**, 220502 (2018).
- [13] V. Tripathi, H. Chen, M. Khezri, K.-W. Yip, E. M. Levenson-Falk, and D. A. Lidar, Suppression of crosstalk in superconducting qubits using dynamical decoupling, *Phys. Rev. Appl.* **18**, 024068 (2022).
- [14] X. Chen, I. Lizuain, A. Ruschhaupt, D. Guéry-Odelin, and J. G. Muga, Shortcut to adiabatic passage in two- and three-level atoms, *Phys. Rev. Lett.* **105**, 123003 (2010).
- [15] E. Torrontegui, S. Ibáñez, S. Martínez-Garaot, M. Modugno, A. del Campo, D. Guéry-Odelin, A. Ruschhaupt, X. Chen, and J. G. Muga, Chapter 2 - shortcuts to adiabaticity, in *Advances in Atomic, Molecular, and Optical Physics*, edited by E. Arimondo, P. R. Berman, and C. C. Lin (Academic Press, 2013), Vol. 62, pp. 117–169.
- [16] A. Vepsäläinen, S. Danilin, and G. Paraoanu, Optimal superadiabatic population transfer and gates by dynamical phase corrections, *Quantum Sci. Technol.* **3**, 024006 (2018).
- [17] A. Vepsäläinen, S. Danilin, and G. S. Paraoanu, Superadiabatic population transfer in a three-level superconducting circuit, *Sci. Adv.* **5**, eaau5999 (2019).
- [18] S. Dogra, A. Vepsäläinen, and G. S. Paraoanu, Experimental demonstration of robustness under scaling errors for superadiabatic population transfer in a superconducting circuit, *Phil. Trans. R. Soc. A* **380**, 20210274 (2022).
- [19] B. T. Torosov and N. V. Vitanov, High-fidelity error-resilient composite phase gates, *Phys. Rev. A* **90**, 012341 (2014).
- [20] S. S. Ivanov and N. V. Vitanov, Composite two-qubit gates, *Phys. Rev. A* **92**, 022333 (2015).
- [21] G. Dridi, M. Mejatty, S. J. Glaser, and D. Sugny, Robust control of a NOT gate by composite pulses, *Phys. Rev. A* **101**, 012321 (2020).
- [22] B. T. Torosov and N. V. Vitanov, High-fidelity composite quantum gates for Raman qubits, *Phys. Rev. Res.* **2**, 043194 (2020).
- [23] B. M. Henson, D. K. Shin, K. F. Thomas, J. A. Ross, M. R. Hush, S. S. Hodgman, and A. G. Truscott, Approaching the adiabatic timescale with machine learning, *Proc. Natl. Acad. Sci. USA* **115**, 13216 (2018).
- [24] M. Bukov, A. G. R. Day, D. Sels, P. Weinberg, A. Polkovnikov, and P. Mehta, Reinforcement learning in different phases of quantum control, *Phys. Rev. X* **8**, 031086 (2018).
- [25] Z. An and D. L. Zhou, Deep reinforcement learning for quantum gate control, *Europhys. Lett.* **126**, 60002 (2019).
- [26] M. Y. Niu, S. Boixo, V. N. Smelyanskiy, and H. Neven, Universal quantum control through deep reinforcement learning, *npj Quantum Inf.* **5**, 33 (2019).
- [27] J. Brown, P. Sgroi, L. Giannelli, G. S. Paraoanu, E. Paladino, G. Falci, M. Paternostro, and A. Ferraro, Reinforcement learning-enhanced protocols for coherent population-transfer in three-level quantum systems, *New J. Phys.* **23**, 093035 (2021).
- [28] F. Sauvage and F. Mintert, Optimal control of families of quantum gates, *Phys. Rev. Lett.* **129**, 050507 (2022).
- [29] L. Giannelli, P. Sgroi, J. Brown, G. S. Paraoanu, M. Paternostro, E. Paladino, and G. Falci, A tutorial on optimal control and reinforcement learning methods for quantum technologies, *Phys. Lett. A* **434**, 128054 (2022).
- [30] Y. Ding, Y. Ban, J. D. Martín-Guerrero, E. Solano, J. Casanova, and X. Chen, Breaking adiabatic quantum control with deep learning, *Phys. Rev. A* **103**, L040401 (2021).
- [31] M.-Z. Ai, Y. Ding, Y. Ban, J. D. Martín-Guerrero, J. Casanova, J.-M. Cui, Y.-F. Huang, X. Chen, C.-F. Li, and G.-C. Guo, Experimentally realizing efficient quantum control with reinforcement learning, *Sci. China Phys. Mech. Astron.* **65**, 250312 (2022).
- [32] A. J. Sirois, M. Castellanos-Beltran, A. E. Fox, S. P. Benz, and P. F. Hopkins, Josephson microwave sources applied to quantum information systems, *IEEE Trans. Quantum Eng.* **1**, 1 (2020).
- [33] G. T. Genov, D. Schraft, T. Halfmann, and N. V. Vitanov, Correction of arbitrary field errors in population inversion of quantum systems by universal composite pulses, *Phys. Rev. Lett.* **113**, 043001 (2014).
- [34] S. Gustavsson, O. Zwiernik, J. Bylander, F. Yan, F. Yoshihara, Y. Nakamura, T. P. Orlando, and W. D. Oliver, Improving quantum gate fidelities by using a qubit to measure microwave pulse distortions, *Phys. Rev. Lett.* **110**, 040502 (2013).
- [35] M. Jerger, A. Kulikov, Z. Vasselin, and A. Fedorov, In situ characterization of qubit control lines: A qubit as a vector network analyzer, *Phys. Rev. Lett.* **123**, 150501 (2019).
- [36] M. A. Rol, L. Ciorciaro, F. K. Malinowski, B. M. Tarasinski, R. E. Sagastizabal, C. C. Bultink, Y. Salathe, N. Haandbaek, J. Sedivy, and L. DiCarlo, Time-domain characterization and correction of on-chip distortion of control pulses in a quantum processor, *Appl. Phys. Lett.* **116**, 054001 (2020).
- [37] J. Kelly, R. Barends, B. Campbell, Y. Chen, Z. Chen, B. Chiaro, A. Dunsworth, A. G. Fowler, I.-C. Hoi, E. Jeffrey, A. Megrant, J. Mutus, C. Neill, P. J. J. O'Malley, C. Quintana, P. Roushan, D. Sank, A. Vainsencher, J. Wenner, T. C. White, A. N. Cleland, and J. M. Martinis, Optimal quantum control using randomized benchmarking, *Phys. Rev. Lett.* **112**, 240504 (2014).
- [38] M. Werninghaus, D. J. Egger, F. Roy, S. Machnes, F. K. Wilhelm, and S. Filipp, Leakage reduction in fast superconducting qubit gates via optimal control, *npj Quant. Inf.* **7**, 14 (2021).
- [39] J. Zeng, C. H. Yang, A. S. Dzurak, and E. Barnes, Geometric formalism for constructing arbitrary single-qubit dynamically corrected gates, *Phys. Rev. A* **99**, 052321 (2019).
- [40] G. Dridi, K. Liu, and S. Guérin, Optimal robust quantum control by inverse geometric optimization, *Phys. Rev. Lett.* **125**, 250403 (2020).
- [41] X. Laforgue, G. Dridi, and S. Guérin, Optimal quantum control robust against pulse inhomogeneities: Analytic solutions, *Phys. Rev. A* **106**, 052608 (2022).
- [42] H.-S. Chang, Y. P. Zhong, A. Bienfait, M.-H. Chou, C. R. Conner, E. Dumur, J. Grebel, G. A. Peairs, R. G. Povey, K. J. Satzinger, and A. N. Cleland, Remote entanglement via adiabatic passage using a tunably dissipative quantum communication system, *Phys. Rev. Lett.* **124**, 240502 (2020).
- [43] A. Sultanov, M. Kuzmanović, A. V. Lebedev, and G. S. Paraoanu, Protocol for temperature sensing using a three-level transmon circuit, *Appl. Phys. Lett.* **119**, 144002 (2021).

- [44] S. Vinjanampathy and J. Anders, Quantum thermodynamics, *Contemp. Phys.* **57**, 545 (2016).
- [45] Y. Lu, A. Bengtsson, J. J. Burnett, B. Suri, S. R. Sathyamoorthy, H. R. Nilsson, M. Scigliuzzo, J. Bylander, G. Johansson, and P. Delsing, Quantum efficiency, purity and stability of a tunable, narrowband microwave single-photon source, *npj Quantum Inf.* **7**, 140 (2021).
- [46] Z. Peng, S. De Graaf, J. Tsai, and O. Astafiev, Tuneable on-demand single-photon source in the microwave range, *Nat. Commun.* **7**, 12588 (2016).
- [47] D. L. Campbell, Y.-P. Shim, B. Kannan, R. Winik, D. K. Kim, A. Melville, B. M. Niedzielski, J. L. Yoder, C. Tahan, S. Gustavsson, and W. D. Oliver, Universal nonadiabatic control of small-gap superconducting qubits, *Phys. Rev. X* **10**, 041051 (2020).
- [48] G. Cao, H.-O. Li, T. Tu, L. Wang, C. Zhou, M. Xiao, G.-C. Guo, H.-W. Jiang, and G.-P. Guo, Ultrafast universal quantum control of a quantum-dot charge qubit using Landau–Zener–Stückelberg interference, *Nat. Commun.* **4**, 1401 (2013).
- [49] L. Wang, T. Tu, B. Gong, C. Zhou, and G.-C. Guo, Experimental realization of non-adiabatic universal quantum gates using geometric Landau-Zener-Stückelberg interferometry, *Sci. Rep.* **6**, 19048 (2016).
- [50] Y. Shapira, J. Markov, N. Akerman, A. Stern, and R. Ozeri, Programmable quantum simulations on a trapped-ions quantum computer with a global drive, *arXiv:2308.16036* (2023).
- [51] G. S. Paraoanu, Microwave-induced coupling of superconducting qubits, *Phys. Rev. B* **74**, 140504(R) (2006).
- [52] C. Rigetti and M. Devoret, Fully microwave-tunable universal gates in superconducting qubits with linear couplings and fixed transition frequencies, *Phys. Rev. B* **81**, 134507 (2010).
- [53] J. Li, K. Chalapat, and G. S. Paraoanu, Entanglement of superconducting qubits via microwave fields: Classical and quantum regimes, *Phys. Rev. B* **78**, 064503 (2008).
- [54] J. M. Chow, A. D. Córcoles, J. M. Gambetta, C. Rigetti, B. R. Johnson, J. A. Smolin, J. R. Rozen, G. A. Keefe, M. B. Rothwell, M. B. Ketchen, and M. Steffen, Simple all-microwave entangling gate for fixed-frequency superconducting qubits, *Phys. Rev. Lett.* **107**, 080502 (2011).
- [55] M. A. Nielsen and I. L. Chuang, *Quantum Computation and Quantum Information: 10th Anniversary Edition* (Cambridge University Press, Cambridge, 2010).
- [56] M. A. Nielsen, A simple formula for the average gate fidelity of a quantum dynamical operation, *Phys. Lett. A* **303**, 249 (2002).
- [57] S. Guérin, V. Hakobyan, and H. R. Jauslin, Optimal adiabatic passage by shaped pulses: Efficiency and robustness, *Phys. Rev. A* **84**, 013423 (2011).
- [58] O. V. Ivakhnenko, S. N. Shevchenko, and F. Nori, Nonadiabatic Landau–Zener–Stückelberg–Majorana transitions, dynamics, and interference, *Phys. Rep.* **995**, 1 (2023).
- [59] L. F. Wei, J. R. Johansson, L. X. Cen, S. Ashhab, and F. Nori, Controllable coherent population transfers in superconducting qubits for quantum computing, *Phys. Rev. Lett.* **100**, 113601 (2008).
- [60] W. D. Oliver, Y. Yu, J. C. Lee, K. K. Berggren, L. S. Levitov, and T. P. Orlando, Mach-Zehnder interferometry in a strongly driven superconducting qubit, *Science* **310**, 1653 (2005).
- [61] M. Sillanpää, T. Lehtinen, A. Paila, Y. Makhlin, and P. Hakonen, Continuous-time monitoring of Landau-Zener interference in a Cooper-pair box, *Phys. Rev. Lett.* **96**, 187002 (2006).
- [62] M. P. Silveri, K. S. Kumar, J. Tuorila, J. Li, A. Vepsäläinen, E. V. Thuneberg, and G. S. Paraoanu, Stückelberg interference in a superconducting qubit under periodic latching modulation, *New J. Phys.* **17**, 043058 (2015).
- [63] A. Abragam, *The Principles of Nuclear Magnetism* (Clarendon, Oxford, 1961).
- [64] N. V. Vitanov, T. Halfmann, B. W. Shore, and K. Bergmann, Laser-induced population transfer by adiabatic passage techniques, *Annu. Rev. Phys. Chem.* **52**, 763 (2001).
- [65] B. W. Shore, Adiabatic states, in *Manipulating Quantum Structures Using Laser Pulses* (Cambridge University Press, Cambridge, 2011), pp. 513–521.
- [66] S. Guérin, S. Thomas, and H. R. Jauslin, Optimization of population transfer by adiabatic passage, *Phys. Rev. A* **65**, 023409 (2002).
- [67] X. Lacour, S. Guérin, and H. R. Jauslin, Optimized adiabatic passage with dephasing, *Phys. Rev. A* **78**, 033417 (2008).
- [68] M. Steffen, J. M. Martinis, and I. L. Chuang, Accurate control of Josephson phase qubits, *Phys. Rev. B* **68**, 224518 (2003).
- [69] L. Van-Damme, D. Schraft, G. T. Genov, D. Sugny, T. Halfmann, and S. Guérin, Robust NOT gate by single-shot-shaped pulses: Demonstration of the efficiency of the pulses in rephasing atomic coherences, *Phys. Rev. A* **96**, 022309 (2017).
- [70] S. Kukita, H. Kiya, and Y. Kondo, Short composite quantum gate robust against two common systematic errors, *J. Phys. Soc. Jpn.* **91**, 104001 (2022).